Electrochemical Characterizations for Oxygen Reduction Reaction of Cobalt-Ferrites Synthesized by Autoignition Process

Disha Soni[1], Rahul Pal[*2] and Raghu Chitta[*3]

[1]*Department of Chemistry, School of Chemical Sciences and Pharmacy, Central University of Rajasthan, Bandarsindri, Ajmer, Rajasthan, India*
[2]*Department of Chemistry, Madanapalle Institute of Technology & Science, Madanapalle, Andhra Pradesh, India*
[3]*Department of Chemistry, National Institute of Technology, Warangal, Telangana, India*
*Corresponding authors: rahulpal@mits.ac.in; raghuchitta@nitw.ac.in

Received 05/05/2025; accepted 05/10/2025
https://doi.org/10.4152/pea.2027450505

Abstract
Cobalt ferrites ($CoFe_2O_4$) for oxygen reduction reaction (ORR) electrocatalytic activity were synthesized by solution combustion synthesis, with varied amounts of borax as additive (10 to 50 at% B). Synthesized catalysts were characterized by X-Ray diffraction, X-Ray Photoelectron Spectroscopy (XPS) and Scanning Electron Microscopy (SEM) techniques. XPS showed the presence of Fe^{3+} and Co^{2+} in prepared samples. Brunauer-Emmet-Teller (BET) isotherms indicated the positive effect of borax as an additive on the surface area. Rotating Disk Electrode (RDE) voltammetry studies indicated that, with increasing amount of borax (10 to 50 at% B), for synthesis of $CoFe_2O_4$, ORR current density increased from 0.15 to 3.56 mA/cm^2. Highest onset potential value of 0.77 V *vs*. reference hydrogen electrode was observed with lower Tafel slope value for FeCo, 10FeCo and 20FeCo, at 66.4, 80.9 and 75 mV/dec, respectively. Koutecky-Levich plot revealed a ~4e ORR process for 20FeCo, which was found to be the best catalyst.

Keywords: borax; cobalt ferrites; electrocatalysis; oxygen reduction reaction; sustainable energy; Tafel plot.

Introduction•

The global energy demand is increasing dramatically due to the rapid soaring need of energy in emerging economies and in human life. However, the limited amount of natural resources, high cost of fossil fuels, ecological and environmental concerns based on fossil fuel consumption have tempted the interest of contemporary research community in finding alternative solutions to meet the worldwide growing energy need [1]. In this regard, electrochemical energy conversion and storage systems have gained much importance owing to their

•The abbreviations list is in page 409.

sustainability. Among these systems, Polymer Electrolyte Membrane Fuel Cells have attracted special attention due to their high energy density and low carbon emissions [2]. However, the key impediment in its commercialization is the utilization of expensive platinum based catalysts for sluggish Oxygen Reduction Reaction (ORR) kinetics at the cathode. Therefore, the development of catalysts with high activity, long-term stability and low cost is of paramount importance to override platinum-based catalysts for ORR [3, 4].

Transition metal oxides are being explored as one of the cheapest alternatives to platinum for electrocatalysis [5]. Mixed transition metal oxides and their nanocomposites, such as Fe and Co, have been extensively used in energy-related applications like super capacitors, [6, 7] lithium ion batteries [8] and fuel cells [2, 5]. Among the catalysts to reduce or replace platinum-based catalysts for ORR, nitrogen-coordinated transition metals in a carbon matrix (M-N-C) have been extensively studied, owing to their extremely effective catalytic activity for ORR, especially in acidic solutions [9, 10]. Single and mixed metal oxides based on Fe, Co, Mn, Zn, Ni, and their composites, with diverse carbon support, such as graphene and carbon nanotubes, have been reported in literature for their efficient electrocatalysis [2, 3, 5, 10-15]. Researchers have reported superior electrocatalytic performance of mixed metal oxides [16- 21].

Various synthetic methodologies have been used for preparing nanomaterials. Solution combustion synthesis method, based on the concept of propellant chemistry, has the advantage of economic and rapid production of fine and homogeneous nanocrystalline powders with high surface area [22-25]. It involves a unique combination of precursors such as metal nitrates as oxidant and a fuel such as urea to yield nanocrystalline metal oxides [22, 25, 26]. Additives incorporated along with precursors during combustion synthesis have been reported to influence structural properties of the final product [27, 28, 29]. Borax as an additive has been reported to promote crystallization process and lower crystallites size during combustion synthesis [30]. Herein, effect of borax as an additive in synthesis of cobalt ferrites ($CoFe_2O_4$) through solution combustion route, and its consequences on the ORR electrocatalytic activity, was investigated.

Experimental

Materials

Structural and chemical measurements

Surface analysis of the samples was performed with the aid of X-ray photoelectron spectrometer (XPS) using ESCA+ (omicron nanotechnology, Oxford Instrument Germany), equipped with monochromator Al K_α (1486.7 eV) source.

Measurement parameters involved 20 and 50 eV pass energy for short and survey scans, respectively. X-ray diffraction (XRD) was performed to examine crystal structure and phase purity of samples. All $CoFe_2O_4$ samples were characterized by XRD at room temperature. Powder samples were analysed within 2θ range from

20 to 80º. Phase identification was carried out by XRD PANalytical Empyrean using Cu K_α radiation, at a scanning rate of 0.02° from $10° \leq \theta \leq 90°$. Surface morphological studies were carried out using SEM JEOL 6010LA (Japan). Brunauer-Emmet-Teller (BET) measurements were carried out using BELSORP MINI II (Japan) analyser. Prior to analysis, the powder sample was oven-air dried at 363 K, for 48 h, and then under flowing nitrogen, for 6 h, at 573 K.

Electrochemical measurements

Electrochemical measurements were performed with Autolab PGSTAT 302N workstation (EcoChemie BV, Netherlands). A three-electrode assembly of Ag/AgCl (reference electrode), platinum wire (counter electrode) and active material (working electrode) formed the electrochemical cell. The working electrode was fabricated by casting a Nafion®-impregnated catalyst ink onto a glassy carbon disc electrode (3 mm diameter). For preparing catalyst ink, 5 µL each Nafion® and isopropanol were mixed with 1 mg of the material and sonicated for 30 min. Then the ink was drop-casted on the glassy carbon electrode and air-dried. Linear Sweep Voltammetry (LSV) and Rotating Disk Electrode (RDE) experiments were performed in an oxygen-saturated 0.5 M H_2SO_4 electrolyte solution at room temperature. Current density reported in this paper is based on the electrode's geometrical disk area. The working electrode was cathodically scanned from 0.8 to -0.2 V (vs Ag/AgCl), at a scan rate of 0.01 Vs^{-1} in all RDE experiments, with varying speed of rotation.

Catalyst preparation

Solution combustion method was employed for $CoFe_2O_4$ synthesis. In a typical synthesis of $CoFe_2O_4$ samples, stoichiometric amounts of $Fe(NO_3)_3$ and $Co(NO_3)_2$ were dissolved in minimum amounts of deionised water, with subsequent addition of urea (amount calculated based on propellant chemistry concept) [22] and borax. The prepared samples were designated as FeCo, 10FeCo, 20FeCo, 35FeCo and 50FeCo, where numerals represent atomic percentage of B from borax added to the starting reaction mixture.

The obtained homogenous solution was neutralized with ammonia, and kept for heating, at around 343 K, until a viscous gel was formed. On temperature increment to 423 K, for 1 h, the gel-like material converted to fine powder, with visible sparks from the reaction mixture. The obtained fine powder was oven-dried and calcined at 773 K, for 2 h.

Results and discussion

X-Ray diffraction

Fig. 1 shows diffraction peaks of $CoFe_2O_4$ with Miller's hkl indices of (111), (220), (311), (400), (422), (511), (333), (440), (533) and (622).

The as-obtained XRD pattern, when compared with $CoFe_2O_4$, indicated cubic phase [31]. Bulk compositions of the samples were found to be unaffected by the

addition of varying amounts of borax during combustion synthesis. Broadening of diffraction peaks can be attributed to smaller crystallite size. Average crystallite size was calculated using Scherrer equation [32], as given below.

$$t = \frac{k\lambda}{\beta s cos\theta} \quad (1)$$

where k = 0.9, λ is wavelength of X-ray, β_s is full-width half maxima (FWHM) and θ is scattering angle.

XRD of a standard silicon sample was recorded prior to measuring samples. In this method, XRD peak fitting was done, and β value was calculated for each fitted peak for β_i and β_t samples. The corrected broadening (β_s) was calculated as:

$$\beta_s = (\beta_t^{\,2} - \beta_i^{2})^{1/2} \quad (2)$$

By inserting β_s value in Scherrer equation, crystallite size was obtained. Average crystallite size was determined after measuring it for each peak, as above, and it was found to be 47, 33, 3 and 5 nm, for FeCo, 20FeCo, 35FeCo and 50FeCo, respectively.

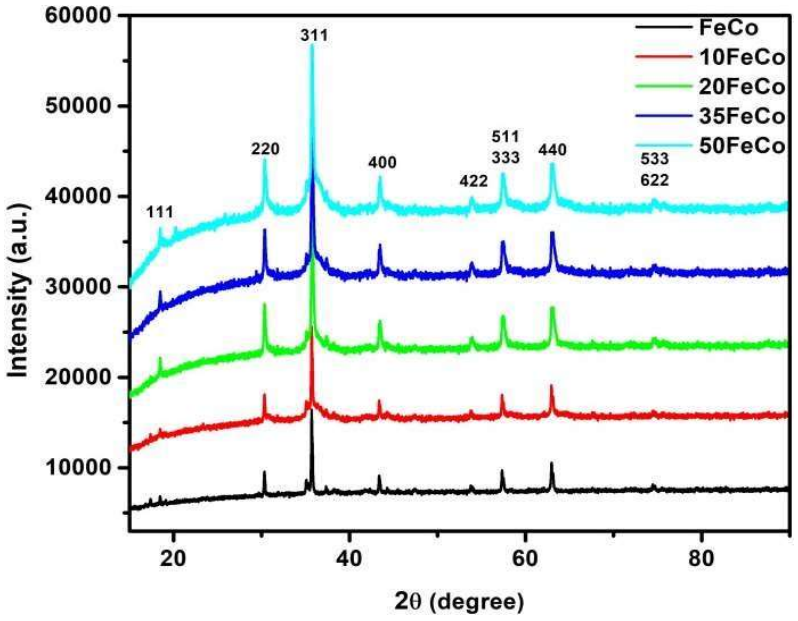

Figure 1: XRD pattern of synthesized $CoFe_2O_4$.

Scanning Electron Microscopy analysis

SEM images of synthesized samples are shown in Fig. 2.

Samples represent agglomerates of irregular shape. From the micrographs, 20FeCo was observed to possess more crystallinity, as compared to FeCo, and well-formed inter-granular pores. On the other hand, FeCo has more flake like layered appearance with pores. 10FeCo represented a lump like surface, whereas 50FeCo surface morphology exhibited low porosity. It can be concluded from SEM micrographs that the catalyst's surface morphology was modified by the effect of borax addition in varying amounts during combustion step.

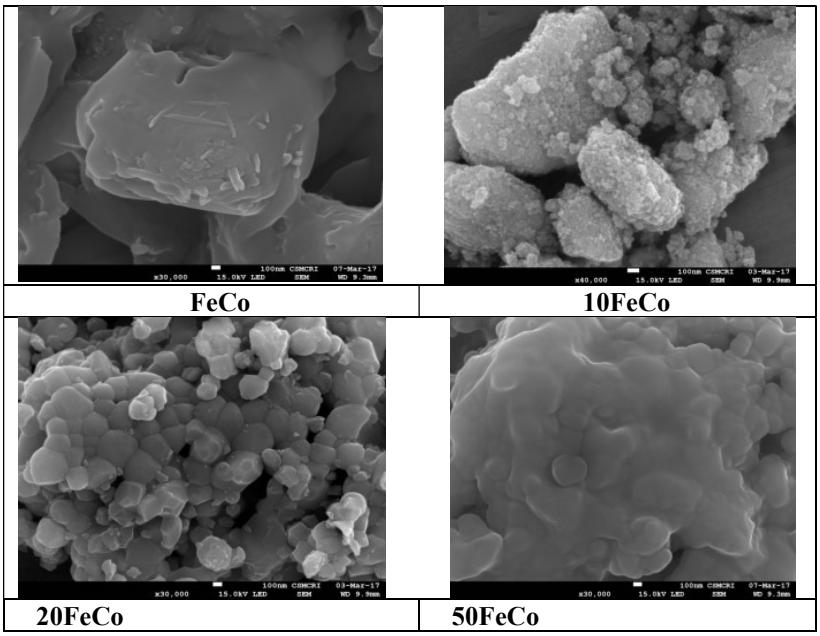

Figure 2: SEM for as-synthesized catalysts.

BET isotherms

Fig. 3 (a) and (b) shows N_2-adsorption desorption isotherms for FeCo and 20FeCo.

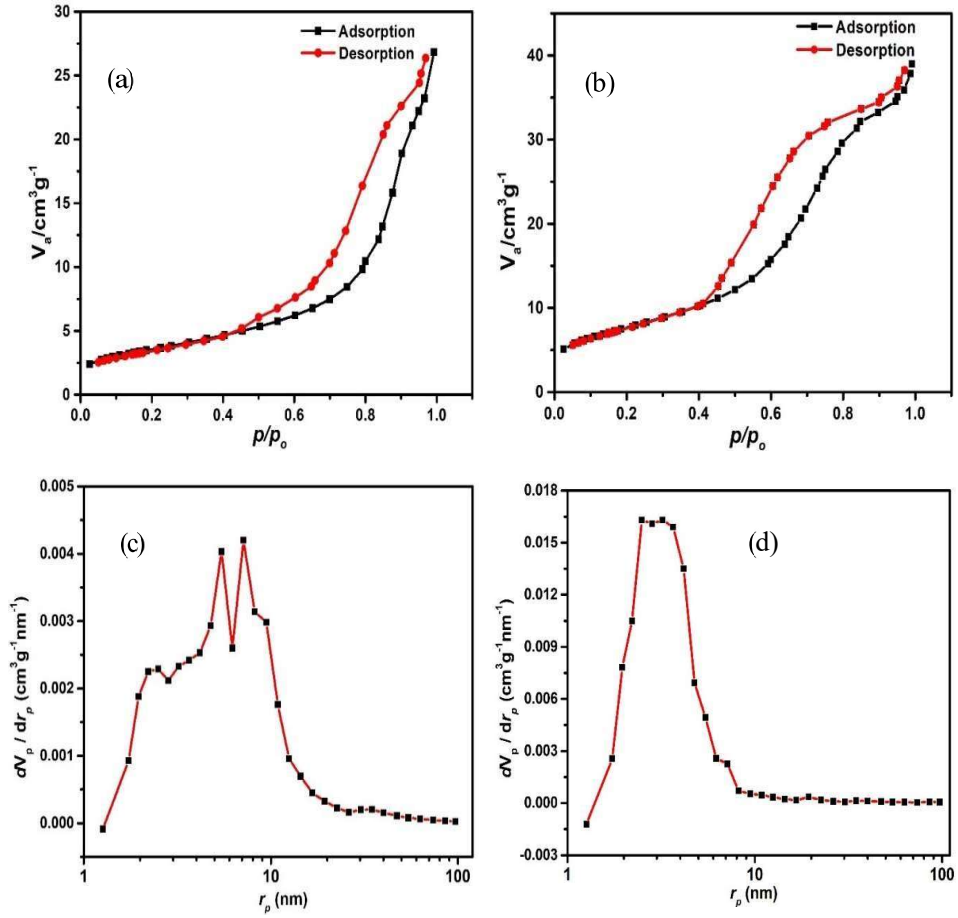

Figure 3: BET isotherm of **(a)** FeCo, **(b)** 20FeCo, and BJH plots for **(c)** FeCo (d) 20FeCo catalysts.

Based on IUPAC classification, [33] adsorption isotherms of both samples were attributed to type IV, with existence of H3 hysteresis loops. A clear hysteresis at high relative pressure was observed, which is related to capillary condensation associated with large pore channels. A sharp inflection appeared in adsorption branch of each isotherm at relative pressure values ranging from 0.4 to 0.7, which indicates capillary condensation in mesopores. Barret-Joyner-Halenda (BJH) plot depicted in Fig. 3(c) demonstrates that, in FeCo, pore diameter was in the range from 2 to10 nm, with highest pore size distribution of ~6 nm. In Fig. 3(d), pore diameters for 20FeCo were found to vary from 2.5 to 4.5 nm, exhibiting maximum distribution along ~2.5 to ~3.7 nm range. Specific surface area of FeCo and 20FeCo was found to be 12.66 and 27.68 cm^2/g^{-1}, respectively. Specific pore volume of FeCo and 20FeCo was determined to be 4.1×10^{-2} and 5.9×10^{-2} cm^3/g, respectively. This incremental effect on surface area was attributed to the use of borax, as reported earlier [34].

Surface elemental analysis

XPS technique was employed for analysing spinels oxidation state and surface chemical composition. XPS survey spectra in Fig. 4 shows Co 2p, Fe 2p and O 1s peaks in synthesized $CoFe_2O_4$ materials. High-resolution spectrum for each element was deconvoluted to gain information related to oxidation state.

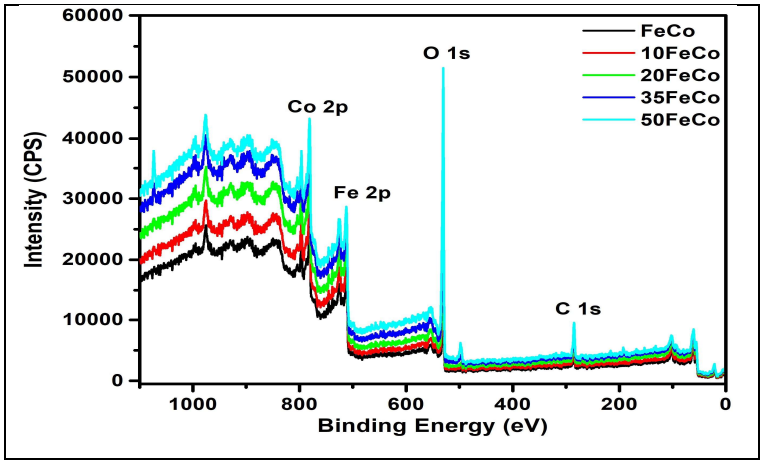

Figure 4: XPS survey spectra of $CoFe_2O_4$.

In FeCo (Fig. 5), Co $2p_{3/2}$ peaks at 779.53 and 781.84 eV were ascribed to Co^{2+}, at octahedral and tetrahedral sites, respectively.

Peaks at binding energy of 794.74 and 796.76 eV are due to Co $2p_{1/2}$ of hkl indices, at octahedral and tetrahedral sites, respectively. Shakeup satellite peaks of Co $2p_{3/2}$ were observed at 785.37 and 789.31 eV [35, 36], while those of Co $2p_{1/2}$ are at 802.14 and 805.39 eV. In Fe 2p region, the presence of two spin orbit doublets, at 710.69 and 712.45 eV of Fe $2p_{3/2}$, suggests occupation of octahedral and tetrahedral sites by Fe^{3+}. Two spin orbit doublets at 723.61 and 726.30 eV are for Fe $2p_{1/2}$ region [36]. Peaks at 731.76 and 717.68 eV are satellite peaks for Fe $2p_{1/2}$ and Fe

$2p_{3/2}$, respectively. These results indicate the presence of Fe^{3+} [35]. Further quantitative analysis of Fe 2p and Co 2p peaks shows Co/Fe atomic ratio of 1:1.5.

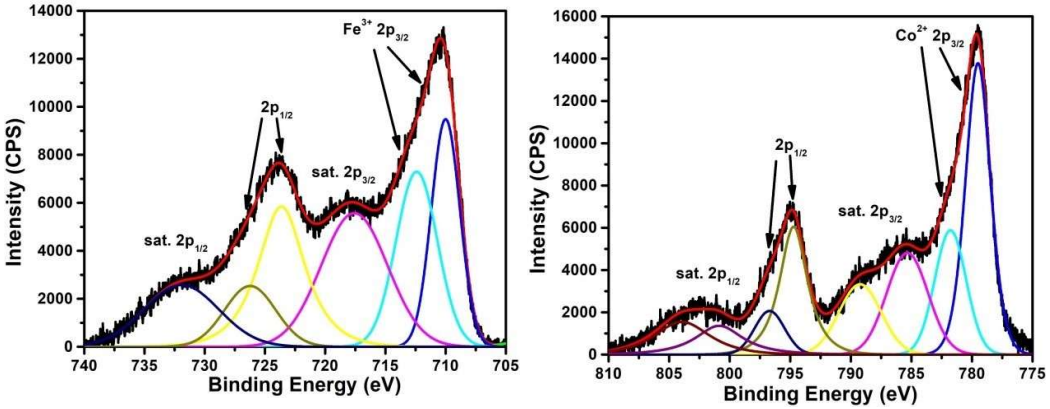

Figure 5: High resolution deconvoluted XPS spectra of **(a)** Fe and **(b)** Co for FeCo.

In 10FeCo (Fig. 6), peaks at binding energy of 782.60 and 797.56 eV represent Co $2p_{3/2}$ and Co $2p_{1/2}$, respectively. Satellite peaks at around 804.34 and 788.19 eV correspond to two shake-up type of Co^{2+}, at high binding energy side of Co $2p_{3/2}$ and Co $2p_{1/2}$ edge, respectively. These indicate the presence of Co^{2+} in the sample. Peaks at 713.06 and 725.77 eV correspond to Fe $2p_{3/2}$ and Fe $2p_{1/2}$ of Fe 2p region, respectively. Peak at 713.06 suggests the presence of Fe^{3+} in tetrahedral position [35]. Peak at binding energy 721.03 eV is satellite peak for Fe $2p_{3/2}$. Co/Fe ratio, as calculated from XPS spectra of 10FeCo, is 1:2.2.

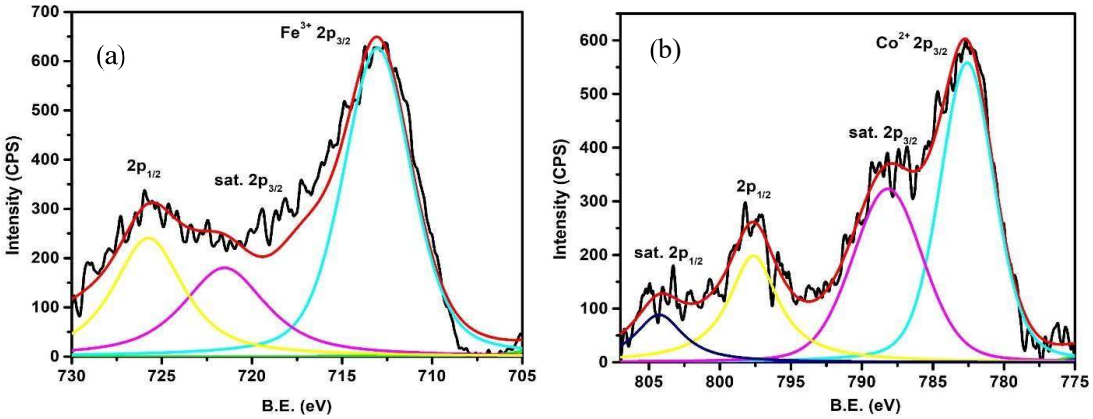

Figure 6: High resolution deconvoluted XPS spectra of **(a)** Fe and **(b)** Co for 10FeCo.

712.34 and 725.38 eV peaks correspond to Fe $2p_{3/2}$ and Fe $2p_{1/2}$, for 20FeCo (Fig. 7). At 717.4 eV, lies satellite peak for Fe $2p_{3/2}$, where Co region was deconvoluted into 4 peaks. Peaks at 781.61 and 797.14 eV are responsible for Co $2p_{3/2}$ and Co $2p_{1/2}$, respectively. Shake-up satellite peaks at 786.76 and 803.29 eV represent Co $2p_{3/2}$ and Co $2p_{1/2}$, respectively. Energy difference of about 4 to 6 eV above Co

$2p_{3/2}$ peak is characteristic of Co^{2+} ion [35-38]. Atomic ratio of Co/Fe was calculated to be 1:0.98, for 20FeCo.

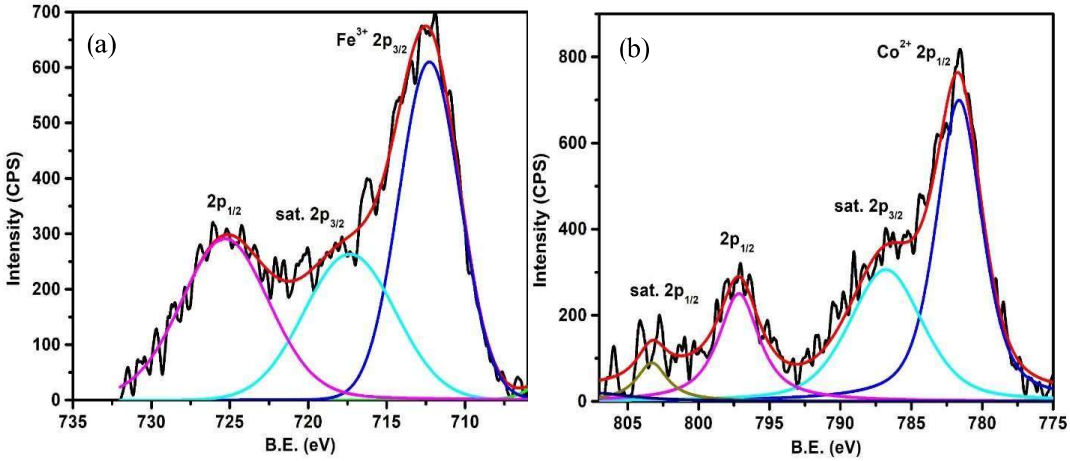

Figure 7: High resolution deconvoluted XPS spectra of **(a)** Fe and **(b)** Co for 20FeCo.

In 35FeCo (Fig. 8), binding energy of 712.29 and 725.04 eV represents Fe $2p_{3/2}$ and Fe $2p_{1/2}$, respectively, and 717.13 eV is satellite peak for Fe $2p_{3/2}$ [36]. Binding energy of 781.88 and 797.09 eV was due to Co $2p_{3/2}$ and Co $2p_{1/2}$, respectively. Binding energy of 786.72 and 803.31 eV correspond to satellite peaks for Co $2p_{3/2}$ and Co $2p_{1/2}$, respectively. Co/Fe ratio for 35FeCo was calculated as 1:1.

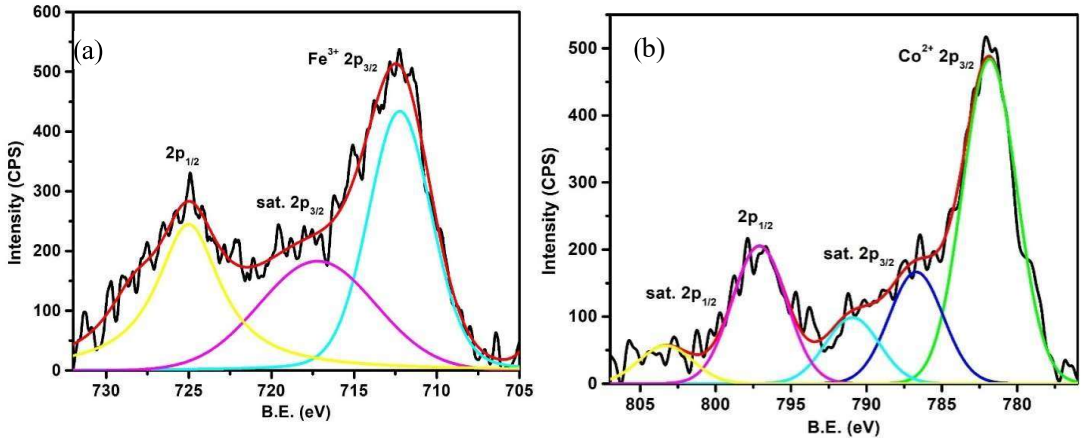

Figure 8: High resolution deconvoluted XPS spectra of **(a)** Fe and **(b)** Co for 35FeCo.

In 50FeCo (Fig. 9), peaks at binding energy of 712.64 eV and 725.50 eV were due to Fe $2p_{3/2}$ and Fe $2p_{1/2}$, respectively. At 718.82 eV lies satellite peak for Fe $2p_{3/2}$. In Co 2p region, peaks associated with binding energy of 781.90 and 796.94 eV were due to Co $2p_{3/2}$ and Co $2p_{1/2}$, respectively. Binding energies of 786.57 and 790.67 eV are assigned as satellite peaks of Co $2p_{3/2}$. Peak at 802.05 eV was due to Co $2p_{1/2}$. Absence of a high-resolution spectrum obtained for Co 2p, around Co^{3+} A-site position (798.5 eV), indicates the presence of Co^{2+} in catalysts [36]. Surface atomic ratio Co/Fe was found to be 1:2.3 for 50FeCo.

Fe and Co 2p and shake-up satellite peaks confirmed +3 and +2 oxidation states of Fe and Co in prepared catalysts, respectively. These results demonstrate that the catalyst has a surface composition of Fe^{3+} and Co^{2+} metal ions. Fe and Co were present in octahedral and tetrahedral sites of the spinel, respectively.

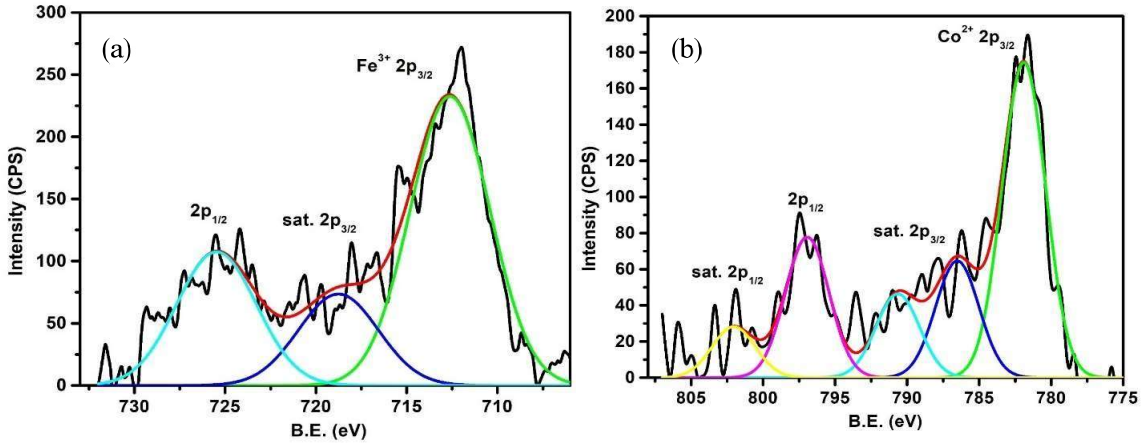

Figure 9: High resolution deconvoluted XPS spectra of **(a)** Fe and **(b)** Co for 50FeCo.

Electrochemical characterization

To assess ORR electrocatalytic activity of synthesized $CoFe_2O_4$, LSV polarization curves were recorded in a nitrogen and oxygen purged 0.5 M H_2SO_4 electrolyte solution (Fig. 10). A substantial cathodic current peak was observed for FeCo catalyst (Fig. 11) in oxygen-saturated electrolyte, as compared to a featureless LSV in nitrogen-saturated electrolyte. This behaviour suggests electrocatalytic activity of as-prepared catalysts towards cathodic ORR.

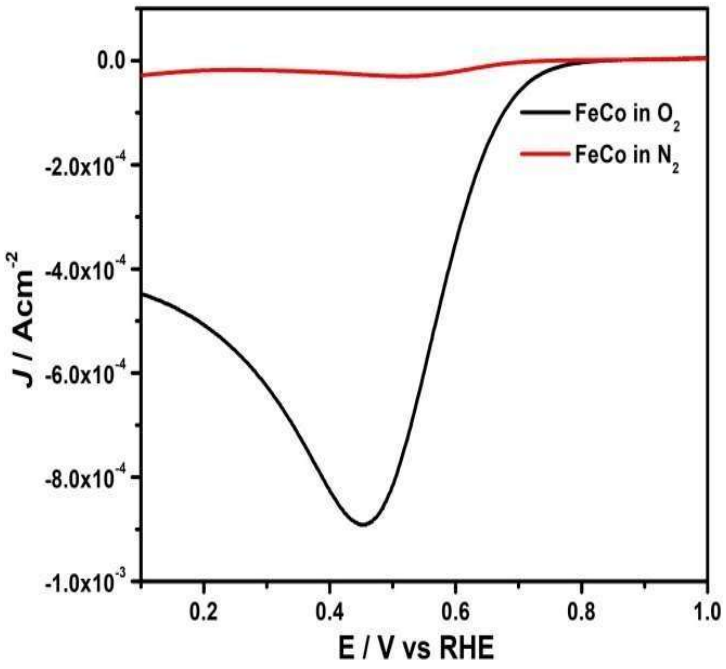

Figure 10: LSV of FeCo in 0.5 M N_2 and O_2-saturated.

RDE voltammograms of all catalysts at various rotation rates are shown in Figs. 11 to 15.

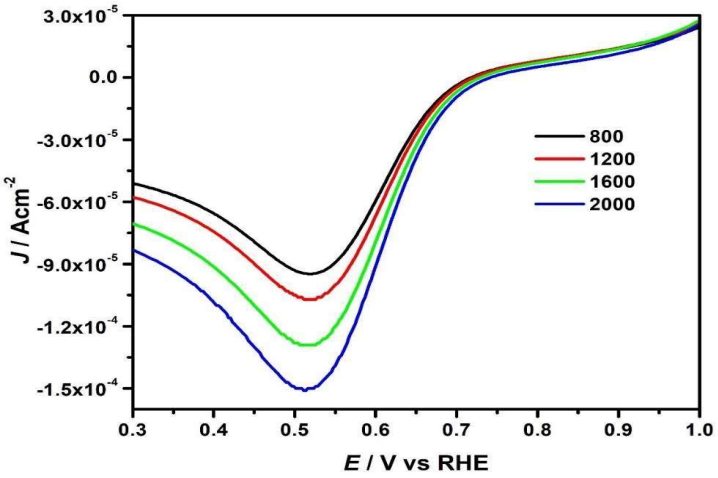

Figure 11: RDE voltammograms of FeCo at various rotation rates in 0.5 M H_2SO_4.

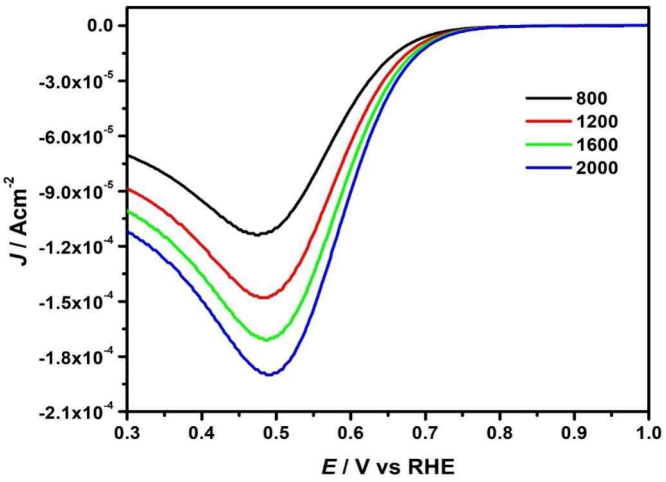

Figure 12: RDE voltammograms of 10FeCo at various rotation rates in 0.5 M H_2SO_4.

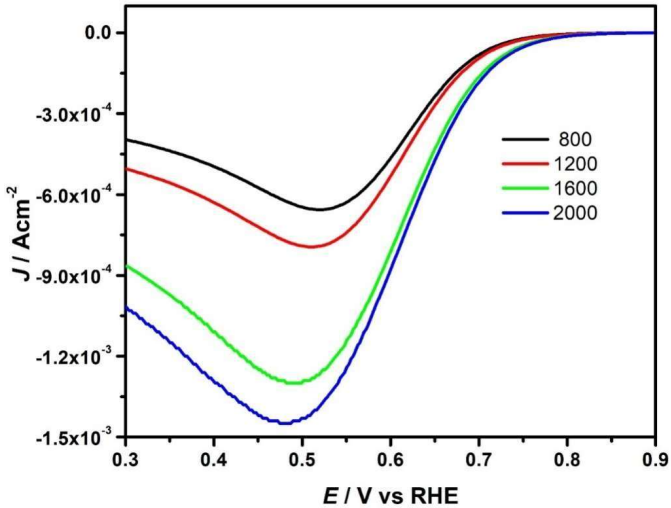

Figure 13: RDE voltammograms of 20FeCo at various rotation rates in 0.5 M H_2SO_4.

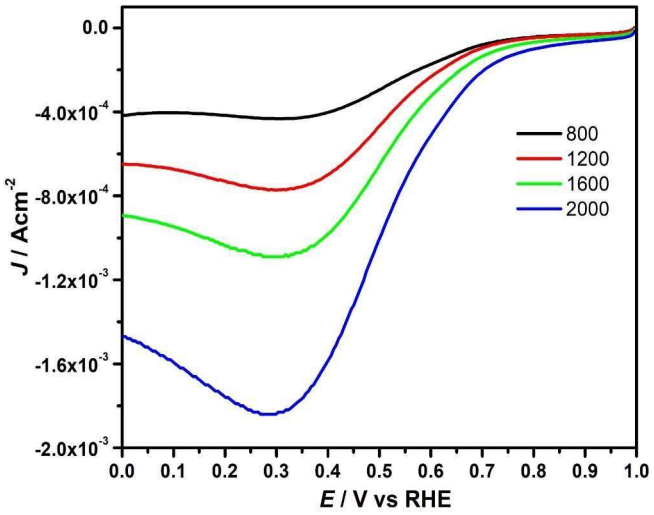

Figure 14: RDE voltammograms of 35FeCo at various rotation rates in 0.5 M H_2SO_4.

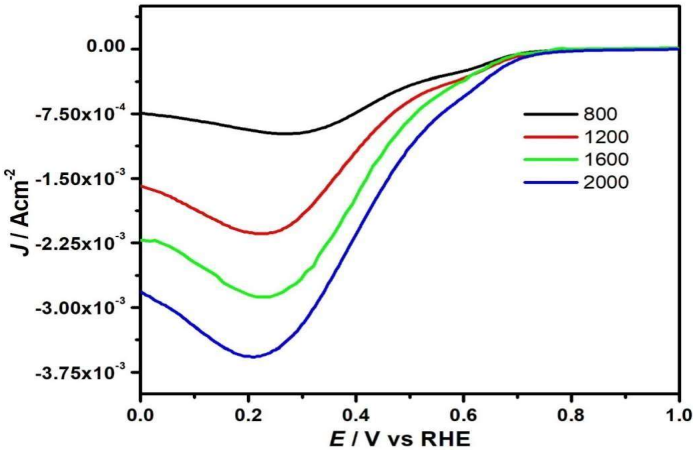

Figure 15: RDE voltammograms of 50FeCo at various rotation rates in 0.5 M H_2SO_4.

RDE polarization curve for each catalyst at 2000 rpm is depicted in Fig. 16.

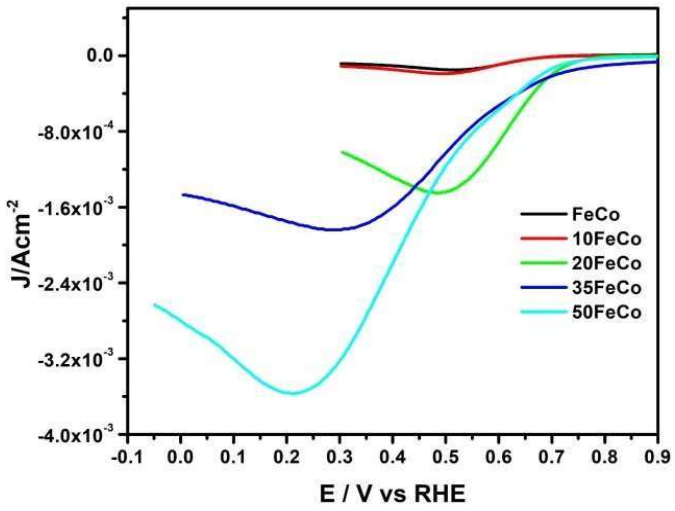

Figure 16: RDE voltammograms of different $CoFe_2O_4$ catalysts at 2000 rpm in 0.5 M H_2SO_4.

Increasing trend of current density from 0.15 to 3.56 mA/cm^2 was observed in ascending order for catalysts labelled FeCo to 50FeCo. This behaviour is accounted to the increase in amount of borax additive from 10 to 50 at% B during synthesis process, indicating that higher quantity of oxygen molecules are adsorbed and reduced on the metal oxide catalyst's surface. This positive trend in current density may be attributed to the incremental effect of surface area, as evident from BET surface area analysis (vide supra).

It is also observed in Fig. 16 that onset potential for ORR is 0.67 V for FeCo and 10FeCo. ORR onset potential shifted to 0.77 V, for 20FeCo, 35FeCo and 50FeCo. This behaviour indicates that borax additive has a beneficial effect on electrocatalytic activity of FeCo spinel.

As evident from onset potential for ORR of these samples, activity order was: FeCo ≈ 10FeCo < 20FeCo ≈ 35FeCo ≈ 50 FeCo. Onset potential is much lower compared to 0.84 to 0.86 V, reported for M–Ti/carbon black (M: Fe, Co) [12] and FeCo/MWCNT electrocatalysts prepared by [11]. Onset potential of ~0.8 V was showed by $Co_xMo_{1-x}N_y$/N-doped carbon nanocage hybrids with $x \geq 0.35$ developed by [13]. ORR peak potential for different $CoFe_2O_4$ in Fig. 16 was observed to be 0.51 and 0.48 V, for FeCo and 20FeCo, respectively. ORR peak potential shifted to much lower values of 0.28 V and 0.21 V, for 35FeCo and 50FeCo, respectively. Here, the increase in peak current is due to the change in number of electrons transferred, in accordance with Eq. (4). Non-involvement of any carbon support material in this present study may be the reason for lower onset potential and higher overpotential. It is surmised that some structural changes might have hindered oxygen adsorption on the catalyst surface and hence catalysis.

The number of electrons transferred during ORR process can be obtained from the analysis of Koutecky-Levich (K-L) plot, which involves following equations [39]:

$$\frac{1}{I} = \frac{1}{I_k} + \frac{1}{I_l} \tag{3}$$

$$I_l = 0.201 nFAC_{O_2} D_{O_2}^{\frac{2}{3}} v^{-\frac{1}{6}} \omega^{\frac{1}{2}} \text{and } I_k = nFkC_0 \tag{4}$$

where I_k and I_l are kinetic and diffusion limiting current, A is electrode area (in cm^2), D is diffusion coefficient, ω is rotation rate in rpm, v is kinematic viscosity of electrolyte solution, C is bulk oxygen concentration in electrolyte, n is number of electrons transferred and k is electron transfer rate constant.

The number of electrons involved in ORR was calculated based on K-L equation from their best linear fitted slopes. Slope of K-L plots for different catalysts (Fig. 17) revealed transfer of ~2e$^-$ for FeCo and 10FeCo. For catalysts labelled 20FeCo and 50FeCo, electrons involved on ORR were calculated to be ~4e$^-$. For 35FeCo, ~3e transfer was accounted for ORR process. It should be noted that four-electron transfer during ORR is desirable for achieving high electrocatalytic efficiency [2]. During 4e$^-$ transfer process in ORR, oxygen is reduced to oxide ion (O^{2-}), which forms H_2O in the presence of H^+ ions at cathode-electrolyte interface. But a 2e$^-$

transfer process in ORR results in formation of peroxide ion, which is detrimental to the electrode catalyst.

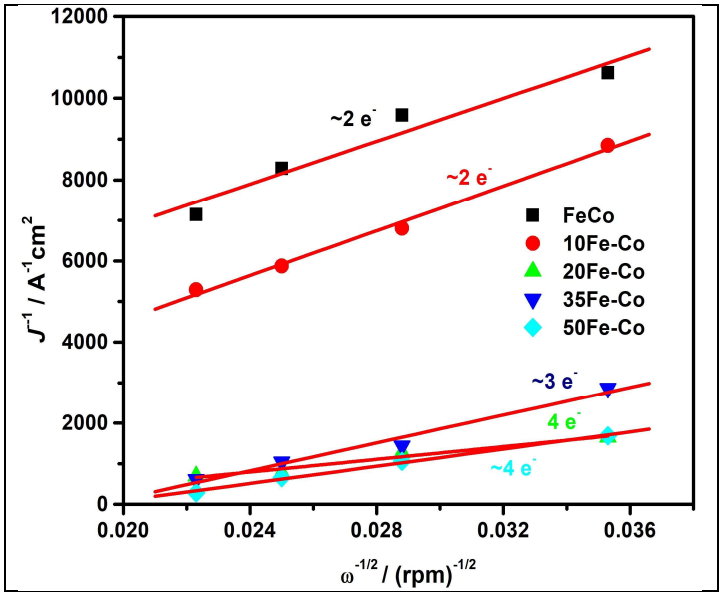

Figure 17: K-L plot derived from RDE voltammograms at various rpm.

Diffusion current corrected Tafel plot was plotted for each catalyst, as shown in Fig. 18. Tafel slopes obtained for different catalysts at 1600 rpm are compared in Table 1. Lower Tafel slope values of 66.4, 80.9 and 75 mV/dec were obtained for FeCo, 10FeCo and 20FeCo, respectively, which signifies faster charge transfer ORR kinetics on these catalysts. However, Tafel slope values of about 233.5 and 149.5 mV/dec, for 35FeCo and 50FeCo, respectively, established sluggish ORR kinetics.

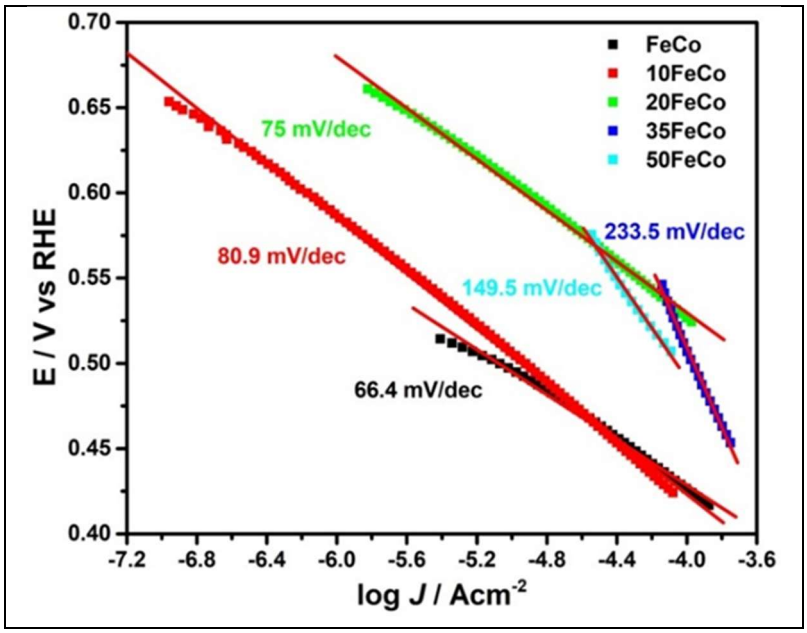

Figure 18: Tafel plot of different catalysts derived from RDE voltammograms at 1600 rpm.

Table 1: Comparison of electrocatalytic parameters for the catalysts.

Catalysts	Tafel slope (mV/dec)	α (charge transfer coefficient)	No. of electrons transferred	I_{ORR} (mA/cm^2)	ORR potential (V)	Onset potential (V)
FeCo	66.38	0.88	~2	0.15	0.51	0.67
10 FeCo	80.87	0.73	~2	0.19	0.49	0.67
20 FeCo	75.02	0.78	~4	1.44	0.48	0.77
35 FeCo	233.46	0.25	~3	1.82	0.28	0.77
50 FeCo	149.45	0.39	~4	3.56	0.21	0.77

Since lower Tafel slope values indicate favourable kinetics, they have been associated with excellent ORR activity. A higher Tafel slope is indicative of the fact that the overpotential increases readily with current density, leading to lower ORR catalytic activity. Lower Tafel slope values for FeCo, 10FeCo, and 20FeCo are comparable to the ones reported in literature. Tafel slopes from 65 to 68 mV/dec^{-1}, for carbon-supported Fe-doped graphitic carbon nitride (Fe-g-C_3N_4@C), have been reported by [14]. Different FeCo-N-rGO materials synthesized by [14] have exhibited Tafel slopes of 81 and 151 mV/dec, respectively. $CoFeN_x$/C catalysts prepared by pyrolysis of cobalt porphyrin and hemin, as reported by [16], indicated a higher Tafel slope of 135 mV/dec. Charge transfer coefficient (α) values are shown in Table 1. The larger value of α signifies higher fraction of interfacial potential at the electrode-H_2SO_4 electrolyte interface, which helps in lowering free energy barrier and hence, creates greater catalytic efficiency. α values were higher for FeCo, 10FeCo and 20FeCo and lower for 35FeCo and 50FeCo spinel oxides.
This study established that the catalyst's surface property overpowers bulk behaviour. XPS and electrochemical analysis of the catalysts, as discussed earlier, established that elemental composition of Fe:Co = 1:0.98, for 20FeCo, showed better ORR performance amongst studied $CoFe_2O_4$.

Conclusions

$CoFe_2O_4$ were synthesized by an economic energy efficient solution combustion method. Borax was added in varied amounts (10 to 50 at% B) during synthesis, to induce crystallization process with low crystallite size. BET surface area results established the effect of borax as an additive. ORR electrocatalytic activity of $CoFe_2O_4$ studied by RDE voltammetry indicated that catalytic current density increased from FeCo onwards to 50FeCo. Lower Tafel slopes and overpotential were observed for FeCo, 10FeCo and 20FeCo. Herein, it was established that among studied catalysts, 20FeCo is superior, due to electrochemical parameters such as lower Tafel slope, higher charge transfer coefficient and lower ORR overpotential.

Acknowledgements

Disha Soni acknowledges CSIR, for Senior Research Fellowship. Raghu Chitta is grateful to Department of Science and Technology (SB/FT/CS-146/2014) and also

for DST-FIST grant (SR/FST/CSi-257/2014(C)) awarded to Department of Chemistry, Central University of Rajasthan. They are thankful to Anirban Paul (CSIR-CSMCRI), for SEM measurements. They acknowledge the support of Dr. Ajit Kumar Patra, Dept. of Physics, Central University of Rajasthan, for XRD measurements, and Materials Research Centre, MNIT Jaipur, for XPS measurements.

Abbreviations

BET: Brunauer-Emmet-Teller
H_2SO_4: Sulphuric acid
K-L: Koutecky-Levich
LSV: Linear Sweep Voltammetry
ORR: Oxygen reduction reaction
RDE: Rotating disk electrode
SEM: Scanning Electron Microscopy
XPS: X-Ray Photoelectron Spectroscopy
XRD: X-Ray diffraction

References

1. Borup R, Meyers J, Pivovar B et al. Scientific aspects of polymer electrolyte fuel cell durability and degradation. Chem Rev. 2007;107(10):3904. https://doi.org/10.1021/cr050182l
2. Othman R, Dicks AL, Zhu Z. Non precious metal catalysts for the PEM fuel cell cathode. Int J Hydrog Ener. 2012;37(1):357. https://doi.org/10.1016/j.ijhydene.2011.08.095
3. Lei H, Shahid Z, Xinlong T et al. Advanced Platinum-Based Oxygen Reduction Electrocatalysts for Fuel Cells. Acc Chem Res. 2021;54(2):311. https://doi.org/.1021/acs.accounts.0c00488
4. Chen Z, Higgins D, Yu A et al. A review on non-precious metal electrocatalysts for PEM fuel cells. Ener Environ Sci. 2011;4(9):3167. https://doi.org/10.1039/C0EE00558D
5. Xia W, Mahmood A, Liang Z et al. Earth-abundant nanomaterials for oxygen reduction. Ang Chem Int Ed. 2016;55(8):2650. https://doi.org/10.1002/anie.201504830
6. Yuan C, Wu HB, Xie Y et al. Mixed transition-metal oxides: Design, synthesis, and energy-related applications. Ang Chem Int Ed. 2014;53(6):1488. https://doi.org/10.1002/anie.201303971.
7. Shi F, Li L, Wang XL et al. Metal oxide/hydroxide-based materials for supercapacitors. RSC Adv. 2014;4(79):41910. https://doi.org/10.1039/C4RA06136E
8. Yu T, Fu J, Cai R et al. Nonprecious Electrocatalysts for Li-Air and Zn-Air batteries: Fundamentals and recent advances. IEEE Nanotechnol Mag. 2017;11(3):29. https://doi.org/10.1109/MNANO.2017.2710380

9. Yuasa M, Yamaguchi A, Itsuki H et al. Modifying carbon particles with polypyrrole for adsorption of cobalt ions as electrocatatytic site for oxygen reduction. Chem Mater. 2005;17(17):4278. https://doi.org/10.1021/CM050958Z
10. Thanh DN, Frenkel AI, Wang J et al. Cobalt–polypyrrole–carbon black (Co–PPY–CB) electrocatalysts for the oxygen reduction reaction (ORR) in fuel cells: Composition and kinetic activity. Appl Catal B. 2011;105(1/2):50. https://doi.org/10.1016/j.apcatb.2011.03.034
11. Lim SH, Li Z, Poh CK et al. Highly active non-precious metal catalyst based on poly(vinylpyrrolidone)–wrapped carbon nanotubes complexed with iron–cobalt metal ions for oxygen reduction reaction. J Pow Sour. 2012;214:15. https://doi.org/10.1016/j.jpowsour.2012.03.094
12. Yin F, Takanabe K, Katayama M et al. Improved catalytic performance of nitrided Co–Ti and Fe–Ti catalysts for oxygen reduction as non-noble metal cathodes in acidic media. Electrochem Commun. 2010;12(9):1177. https://doi.org/10.1016/j.elecom.2010.06.012
13. Sun T, Wu Q, Che R et al. Alloyed Co–Mo nitride as high-performance electrocatalyst for oxygen reduction in acidic medium. ACS Catal. 2015;5(2):1857. https://doi.org/10.1021/cs502029h
14. Wang MQ, Yang WH, Wang HH et al. Pyrolyzed Fe–N–C composite as an efficient non-precious metal catalyst for oxygen reduction reaction in acidic medium. ACS Catal. 2014;4(11):3928. https://doi.org/10.1021/cs500673k
15. Fu X, Liu Y, Cao X et al. FeCo–N_x embedded graphene as high performance catalysts for oxygen reduction reaction. Appl. Catal. B. 2013;130-131:143-151. https://doi.org/10.1016/j.apcatb.2012.10.028
16. Jiang R, Chu D. Comparative study of $CoFeN_x$/C catalyst obtained by pyrolysis of hemin and cobalt porphyrin for catalytic oxygen reduction in alkaline and acidic electrolytes. J Pow Sour. 2014;245:352. https://doi.org/10.1016/j.jpowsour.2013.06.123
17. Huo R, Jiang WJ, Xu S et al. Co/CoO/$CoFe_2O_4$/G nanocomposites derived from layered double hydroxides towards mass production of efficient Pt-free electrocatalysts for oxygen reduction reaction. Nanoscale. 2014;6(1):203. https://doi.org/10.1039/C3NR05352K
18. Indra A, Menezes PW, Sahraie NR et al. Unification of catalytic water oxidation and oxygen reduction reactions: Amorphous beat crystalline cobalt iron oxides. J Amer Chem Soc. 2014;136(50):17530. https://doi.org/10.1021/ja509348t
19. Toh RJ, Sofer Z, Pumera M. Transition metal oxides for the oxygen reduction reaction: influence of the oxidation states of the metal and its position on the periodic table. Chem Phys Chem. 2018;16(16):3527. https://doi.org/10.1002/cphc.201500483

20. An L, Jiang N, Li B et al. A highly active and durable iron/cobalt alloy catalyst encapsulated in N-doped graphitic carbon nanotubes for oxygen reduction reaction by a nanofibrous dicyandiamide template. J Mater Chem. 2018;6(14):5962. https://doi.org/10.1039/C8TA01247D
21. Zhao YM, Wang FF, Wei PJ et al. Cobalt and iron oxides co-supported on carbon nanotubes as an efficient bifunctional catalyst for enhanced electrocatalytic activity in oxygen reduction and oxygen evolution reactions. 2018;3(1):207. https://doi.org/10.1002/slct.201702231
22. Sutka A, Mezinskis G. Sol-gel auto-combustion synthesis of spinel-type ferrite nanomaterials. Front Mater. Sci. 2012;6:128. https://doi.org/10.1007/s11706-012-0167-3
23. Costa ACFM, Morelli MR, Kiminami RHGA. Microstructure and magnetic properties of Ni_{1-x} $Zn_xFe_2O_4$ synthesized by combustion reaction. J Mater Sci. 2007;42:779. https://doi.org/10.1007/s10853-006-1440-6
24. George, Mary John A, Nair SS et al. Finite size effects on the structural and magnetic properties of sol–gel synthesized $NiFe_2O_4$ powders. J Magn Magn Mater. 2006;302(1):190. https://doi.org/10.1016/j.jmmm.2005.08.029
25. Mukasyan AS, Epstein P, Dinka P. Solution combustion synthesis of nanomaterials. Proc Combust Inst. 2007;31(2):1789. https://doi.org/10.1016/j.proci.2006.07.052
26. Li FT, Ran J, Jaroniec M et al. Solution combustion synthesis of metal oxide nanomaterials for energy storage and conversion. Nanoscale. 2015;7(42):17590. https://doi.org/10.1039/C5NR05299H
27. Varma A, Mukasyan AS, Rogachev AS et al. Solution combustion synthesis of nanoscale materials. Chem Rev. 2016;116(3):14493. https://doi.org/10.1021/acs.chemrev.6b00279
28. Gao Y, Meng F, Cheng Y et al. Influence of fuel additives in the urea-nitrates solution combustion synthesis of Ni-Al_2O_3 catalyst for slurry phase CO methanation. Appl Catal A. 2017;534:12. https://doi.org/10.1016/j.apcata.2017.01.016
29. Chourashiya MG, Urakawa A. Solution combustion synthesis of highly dispersible and dispersed iridium oxide as an anode catalyst in PEM water electrolysis. J Mater Chem A. 2017;5(10):4774. https://doi.org/10.1039/C6TA11047A
30. Fellinger TP, White RJ, Titirici MM et al. Borax-mediated formation of carbon aerogels from glucose. Adv Funct Mater. 2012;22(15):3254. https://doi.org/10.1002/adfm.201102920
31. Blasco J, Subías G, García J et al. High-pressure transformation in the cobalt spinel ferrites. J Solid State Chem. 2015;221(8):173. https://doi.org/10.1016/j.jssc.2014.09.028
32. Patterson AL. The Scherrer formula for X-Ray particle size determination. Phys Rev. 1939:56;978. https://doi.org/10.1103/PhysRev.56.978

33. Thommes M, Kaneko K, Neimark AV et al. Physisorption of gases, with special reference to the evaluation of surface area and pore size distribution (IUPAC Technical Report). Pure and Appl Chem. 2015;87(9-10):1051. https://doi.org/10.1515/pac-2014-1117
34. Jiang GJ, Xu JY, Shen H et al. Fabrication and properties of zinc silicate phosphors through solid state reaction. Adv Mater Res. 2010;160-162:594-598. https://doi.org/10.4028/www.scientific.net/AMR.160-162.594
35. Zhou Z, Zhang Y, Wang Z et al. Electronic structure studies of the spinel $CoFe_2O_4$ by X-ray photoelectron spectroscopy. Appl Surf Sci. 2008;254(21):6972. https://doi.org/10.1016/j.apsusc.2008.05.067
36. Zhu K, Jin C, Klencsár Z et al. Cobalt-iron oxide, alloy and nitride: Synthesis, characterization and application in catalytic peroxymonosulfate activation for Orange II degradation. Catalysts. 2017;7(5):138. https://doi.org/10.3390/CATAL7050138
37. Magno de LAT, Amorim BF, Morales TMA et al. Waspwaisted behavior in magnetic hysteresis curves of $CoFe_2O_4$ nanopowder at a low temperature: experimental evidence and theoretical approach. RSC Adv. 2017;7(36):22187. https://doi.org/10.1039/C6RA28727A
38. Tholkappiyan R, Vishista K. Tuning the composition and magnetostructure of dysprosium iron garnets by Co-substitution: An XRD, FT-IR, XPS and VSM study. Appl Surf Sci. 2015;351:1016. https://doi.org/10.1016/j.apsusc.2015.05.193
39. Bard AJ, Faulkner LR. Electrochemical Methods: Fundamentals and Applications. J. Wiley and Sons, New York. 2000.